JACS
JOURNAL OF THE AMERICAN CHEMICAL SOCIETY

ARTICLE

pubs.acs.org/JACS

Dynamic Solubility Limits in Nanosized Olivine $LiFePO_4$

Marnix Wagemaker,[*,†] Deepak P. Singh,[†] Wouter J.H. Borghols,[†,‡] Ugo Lafont,[†] Lucas Haverkate,[†] Vanessa K. Peterson,[§] and Fokko M. Mulder[†]

[†]Faculty of Applied Sciences, Delft University of Technology, The Netherlands

[‡]Institut für Festkörperforschung, Forschungszentrum Jülich GmbH, Jülich Centre for Neutron Science at FRM II, 85747 Garching, Germany

[§]Australian Nuclear Science & Technology Organization, Bragg Institute, Menai, NSW 223, Australia

Supporting Information

ABSTRACT: Because of its stability, nanosized olivine $LiFePO_4$ opens the door toward high-power Li-ion battery technology for large-scale applications as required for plug-in hybrid vehicles. Here, we reveal that the thermodynamics of first-order phase transitions in nanoinsertion materials is distinctly different from bulk materials as demonstrated by the decreasing miscibility gap that appears to be strongly dependent on the overall composition in $LiFePO_4$. In contrast to our common thermodynamic knowledge, that dictates solubility limits to be independent of the overall composition, combined neutron and X-ray diffraction reveals strongly varying solubility limits below particle sizes of 35 nm. A rationale is found based on modeling of the diffuse interface. Size confinement of the lithium concentration gradient, which exists at the phase boundary, competes with the in bulk energetically favorable compositions. Consequently, temperature and size diagrams of nanomaterials require complete reconsideration, being strongly dependent on the overall composition. This is vital knowledge for the future nanoarchitecturing of superior energy storage devices as the performance will heavily depend on the disclosed nanoionic properties.

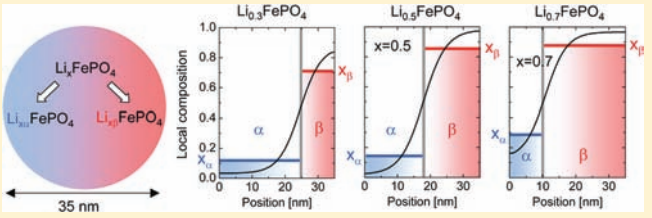

INTRODUCTION

Application of Li-ion batteries in hybrid and electrical vehicles is emerging pending improved performance, cost, and safety. This has initiated worldwide research for better Li-ion electrode materials that combine desirable properties such as high energy density, low cost, and electrochemical stability. For this reason, Li_xFePO_4 ($0 < x < 1$), proposed by Padhi et al.[1] in 1997, has received considerable attention. The initial hurdle of poor intrinsic electronic conduction was overcome using small particles in combination with conductive phases.[2,3] The next improvement, nanosizing in combination with ionic conducting phases, resulted in unexpected fast kinetics.[4] The general fundamental question is: are the improvements simply due to the trivial shorter diffusion distances, or does nanosizing alter critical materials properties such as defect chemistry and the two-phase Li-insertion behavior in a nontrivial way. A direct observation is the smearing out of the voltage plateau for nanosized insertion materials, indicating a distribution in nano particle size,[5,6] and/or a smearing out of the first-order phase transition as the result of configurational entropy.[7] In particular the two-phase versus single-phase insertion reaction in $LiFePO_4$ has been under intensive research,[8−16] demonstrating narrow solid solution domains in micrometer sized particles at room temperature[12] and a solid solution over the entire compositional range above 520 K.[8,17] Yamada et al.[12] reported extended solid-solution-composition-ranges in small particles, and a systematic decrease of the miscibility gap was suggested based on Vegard's law.[16] Kobayashi et al.[11] isolated solid solution phases also supporting a size-dependent miscibility gap. This indicates not only altered thermodynamics in nanosized insertion materials but also implies altered kinetics because the local concentration will strongly affect the diffusion coefficient[18−20] and the lattice mismatch, which may also change the phase-transition kinetics.[10] Interestingly, these size-dependent phenomena appear to be a general phenomenon for two-phase intercalation systems as indicated by results on Li_xTiO_2 and MgH_x systems.[21−23]

Theoretical work indicates the importance of the diffuse interface,[13] strain,[10,24] and interface energy[14] that will increase the energy of the coherent interface between the coexisting phases. Although strain and interface energy are expected to cause larger solid-solution-composition-ranges, the solubility limits are predicted to be almost unaffected when the two phases coexist.[11] In contrast, Burch et al.[13] showed that in theory the diffuse interface is able to destabilize the two-phase coexistence predicting a size-dependent miscibility gap.[13] The diffuse interface also appeared an essential ingredient for the prediction[25] of the experimentally observed layer-by-layer intercalation in $LiFePO_4$[26−28] (domino-cascade model[26]).

Received: March 23, 2011
Published: May 20, 2011

dx.doi.org/10.1021/ja2026213 | J. Am. Chem. Soc. 2011, 133, 10222–10228

Here, we present a systematic study revealing the impact of particle size and composition on the miscibility gap in nanosized $LiFePO_4$. This is accomplished by using neutron diffraction which allows direct determination of the partial Li occupancies on the 4a site in coexisting heterosite $Li_{x\alpha}FePO_4$ and triphylite $Li_{x\beta}FePO_4$ phases and direct comparison with thermodynamical calculations based on the diffuse interface. The most intriguing finding is that the miscibility gap in small particles not only shrinks, but also strongly depends on the overall composition. Hence the miscibility gap is not constant during (dis)charge, in contrast to our common knowledge based on bulk materials. In stead the solubility limits in nanosized Li_xFePO_4 depend strongly on the state-of-charge. Direct comparison with model calculations of the diffuse interface rationalizes the observed dependence of the solubility limits on the overall composition, showing excellent agreement with the experimental size-dependent solubility limits. This new insight in the thermodynamics of nanoinsertion materials also implies that the Li-ion kinetics and phase transitions in these nanosized materials will be very different from that in bulk materials.

Different crystallite sizes, 22 ± 8, 25 ± 8, 35 ± 10, 70 ± 18, and 140 ± 20 nm, were prepared by ball-milling resulting in agglomerated crystallites shown in part b of Figure 1. TEM indicates only a very small amorphous fraction and a limited crystallite size distribution based on 100−200 crystallites. Various compositions Li_xFePO_4 between $x = 0$ and $x = 1$ were prepared by chemical delithiation (NO_2BF_4) and subsequent lithiation (butyllithium) leading to the coexistence of the distinct Li-poor triphylite and Li-rich heterosite phases, here referred to as α-phase and β-phase, respectively. To avoid confusion, we will refer to the initial crystallite size as the particle size. Because oxidation of the materials may be expected,[11] the materials were prepared and stored under argon atmosphere. Neutron and X-ray diffraction data were obtained at room temperature and simultaneously refined in the *Pnma* space group for both the Li-poor (α) heterosite $Li_{x\alpha}FePO_4$ and the Li-rich (β) triphylite $Li_{x\beta}FePO_4$ phases, where x_α and x_β indicate the lithium compositions in the two phases. The size broadening is in excellent agreement with the average size observed by TEM. The combined use of X-ray and neutrons permitted to establish that no significant amounts of anti site defects are present, which excludes this as a possible cause for the observed solid solution behavior.[29]

Anisotropic strain parameters were required to obtain accurate fits, which could be distinguished from the isotropic size broadening due to the large *d*-spacing range of the TOF neutron diffraction data. This implies that the two phases coexist within one particle, which was further confirmed by additional size broadening of the two coexisting phases, as seen in the Supporting Information. For different particle sizes having overall composition $Li_{0.5}FePO_4$ the resulting anisotropic strain is shown in part c of Figure 1 indicating largest strain in the *bc* plane consistent with the orientation of the interface between the two phases perpendicular to the *a* axis as shown by Chen et al.[27] Interestingly, the anisotropic strain is much larger for smaller particles, most likely indicating that in smaller particles a larger fraction of the material experiences strain. This will be a consequence of particle size, in smaller particles the material is on average closer to the interface, the interface causing the strain due to the lattice mismatch. The large strain also indicates that the interfaces in the nanoparticle sizes remain coherent: the limited length scale of the interface apparently prevents crack forming, which occurs in larger particles to relax the large misfit between the two lattices.[27] Accurate refinement of the Li-occupancies necessitates fitting of anisotropic displacement parameters (ADP's). The ellipsoid shaped ADP's in part d of Figure 1 indicate a curved diffusion path of the Li-ions in the *b* direction, in line with the results obtained by Nishimura et al.[30] and consistent with predictions based on DFT calculations.[31,32] Also note that the disorder of the PO_4 groups indicates some degree of rotational freedom. This disorder, as quantified by the value of the ADP's was significantly larger for smaller particle sizes. This indicates a larger degree of structural disorder for smaller particle sizes, which is most likely indicative of changes in the Li-occupancies as is discussed below.

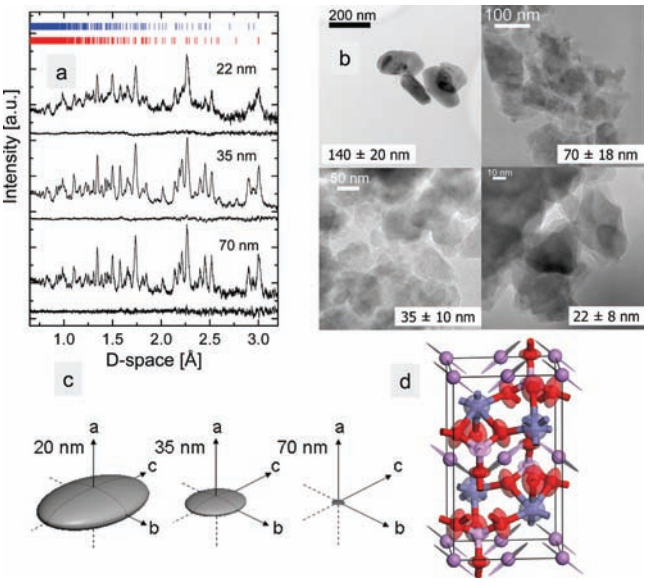

Figure 1. Neutron diffraction patterns, TEM, strain, and anisotropic temperature factors. (a) Neutron diffraction patterns for three different particle sizes all having overall composition $Li_{0.5}FePO_4$. (b) TEM of different particle sizes prepared by ball milling. The size indicates the average size and width of the crystallite size distribution based on approximately 150 crystallites. (c) Anisotropic strain broadening for different particle sizes resulting from simultaneous Rietveld refinement of neutron and X-ray diffraction data. (d) $LiFePO_4$ unit cell showing the anisotropic displacement factors resulting from the simultaneous Rietveld refinement of neutron and X-ray diffraction data. For display purposes the displacement factors are multiplied by a factor of 15.

The reduced difference in the Li-density between the coexisting phases in the Fourier-density-difference-maps shown in Figure 2, based on the neutron diffraction data, points toward a shrinking miscibility gap for smaller particle sizes. This is quantitatively shown in part a of Figure 3, which is the first direct proof of the reduction of the miscibility gap in $LiFePO_4$. This is based on materials having an overall composition $Li_{0.5}FePO_4$, hence inside the two-phase region, complementary to the reduced miscibility gap in the solid solution composition domain previously shown.[11,16] In the same part a of Figure 3, the relative changes in cell volume of both phases are observed to be much smaller than the relative changes in the solubility limits. This demonstrates that Vegard's law is not obeyed within the miscibility gap, $x_\alpha < x < x_\beta$, when the two phases coexist, as seen in part a of Figure 4. This should not be considered a surprise because at the bimodal point Vegard's law only applies in very exceptional cases.[33] This is not in contradiction but is complementary to the results of Kobayashi et al.,[11] who reported the

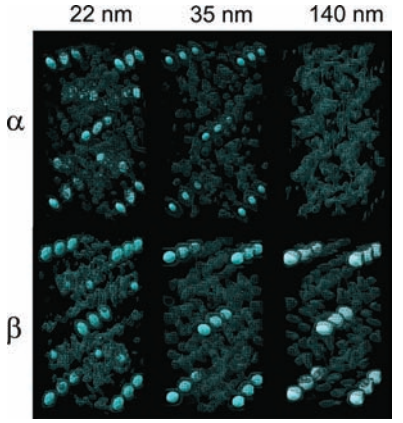

Figure 2. Fourier density difference maps. Fourier density difference maps of both the Li-poor α−phase and the Li-rich β-phase in $Li_{0.5}FePO_4$ in the three different particle sizes indicated. The Fourier maps were obtained by Fourier transform of the difference between the neutron diffraction data and the calculated diffraction pattern based on the unit cell with no Li-ions present. Therefore, these density maps should disclose the Li-ion density. As expected for large particles, large Li-ion density is observed in the Li-rich heterosite β-phase, and basically no density is observed in the Li-poor triphylite α−phase. Progressive particle size reduction decreases observed Li-ion density in the heterosite β and more evident increases in the triphylite α phase, indicating a reduction of the miscibility gap with decreasing particle size.

validity of Vegard's law in the solid-solution-compositional-range outside the miscibility gap, overall composition x either $x < x_\alpha$ or $x > x_\beta$.

Having established that the miscibility gap reduces with decreasing particles size, the question is: What is the origin of this fundamental change in the thermodynamics upon particle size reduction? Meethong et al.[16] argued that the strain mediated by the coherent interface, causing compressive stress on the triphylite phase and tensile stress on the heterosite phase, may result in the reduction of the miscibility gap. And because the strain is larger for smaller particles, as confirmed by part c of Figure 1, this qualitatively explains the smaller miscibility gap with decreasing particle size as shown in part a of Figure 3. However, because the change in equilibrium composition is much larger than that of the cell volume, as seen in part a of Figure 3 and part a of 4, there must be an additional mechanism. Burch et al.[13] took into account the free energy due to concentration gradients at the coherent phase boundary, introduced by Cahn and Hillard.[34] Their results predict that the confinement of the diffuse interface due to particle size reduction cause a shrinking miscibility gap[13] in qualitative agreement with our experimental results. For direct comparison with our experimental results, we performed similar calculations as Burch et al.[13] assuming the free energy of mixing is well approximated by the Cahn−Hilliard functional:

$$G_{\mathrm{mix}} = \int_V \left(g_{\mathrm{hom}}(c) + \frac{1}{2}(\nabla c) K (\nabla c) \right) \rho \mathrm{d}V \qquad (1)$$

where $g_{\mathrm{hom}}(c)$ represents the homogeneous free energy here assumed to be a regular solution, c the Li concentration, V the volume, and ρ the density of intercalation sites per unit volume. K is the gradient energy penalty tensor, assuming it is constant independent of the concentration c and the spatial position. Without the contribution to the energy of mixing of the concentration gradient, $K = 0$, the solubility limits follow from the equilibrium conditions leading to the common tangent construction.[35]

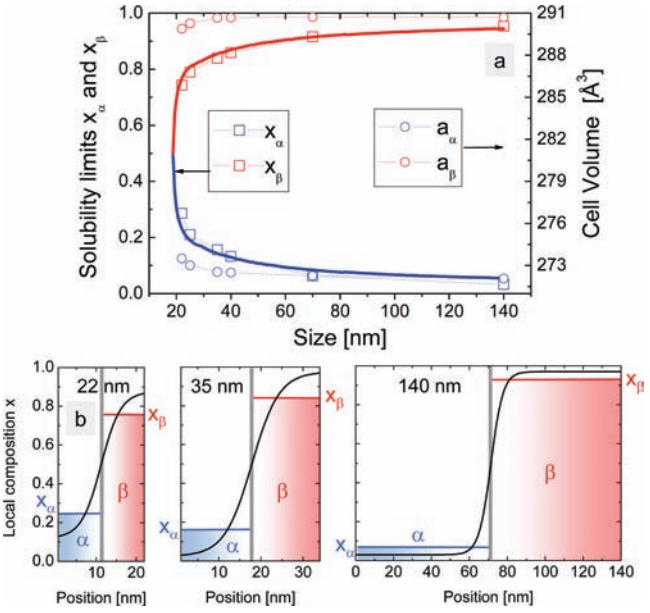

Figure 3. Measured and calculated solubility limits as a function of particle size. (a) Symbols: Fractional lithium occupancy for both the Li-poor triphylite α-phase $Li_{x\alpha}FePO_4$ and the Li-rich heterosite β-phase $Li_{x\beta}FePO_4$ where x_α and x_β represent the average solubility limits (ASL's) as a function of particle size having an overall composition $Li_{0.5}FePO_4$. V_α and V_β represent the corresponding unit cell volume. The size of the symbols is approximately the size of the error. Lines: Calculated average compositions based on the diffuse interface model. (b) Calculated concentration profiles based on the diffuse interface model in the a direction for three different particle sizes at the overall composition $Li_{0.5}FePO_4$. The compositions x_α and x_β represent the average Li-compositions, referred to as average solubility limits (ASL) in the text, in the Li-poor triphylite α-phase and Li-rich heterosite β-phase respectively.

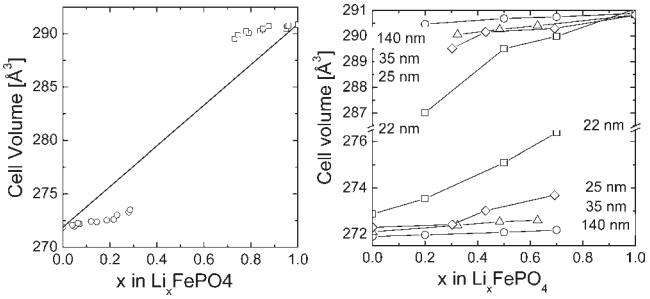

Figure 4. Unit cell volume changes. (a) Comparison of the unit cell volume as a function of the average lithium concentration in the individual phases for samples having coexisting phases (overall composition in the miscibility gap) for both Li-poor (α) (small unit cell) and Li-rich (β) (large unit cell) compared to Vegard's law. (b) Unit cell volume of the Li-poor triphylite α-phase and the Li-rich heterosite β-phase as a function of the overall composition for different particle sizes.

Experimental evidence in Li_xFePO_4 shows the phase boundary is always in the bc plane,[27] as confirmed by the observed anisotropic strain broadening in part c of Figure 1, minimizing its elastic energy.[24,27] As a consequence, the concentration can be

assumed to vary only in the *a* direction, in which the interphasial width was observed to be approximately 4 nm.[27,28] This allows estimating *K* that reduces to a scalar for this 1D case. Consequently, for the calculations only the particle dimension in the *a* direction is relevant, which we will simply refer to as the particle size, thereby implicitly assuming cubic particles. It should be noted that this approach is only valid for coherent interfaces, that is, the particles are sufficiently small that no (destructive) relaxation in the *bc* plane takes place. Further details of the presented calculations can be found in the Supporting Information. It should be realized that by using the experimentally determined interphasial width to determine the energy penalty *K* the latter includes both the effect of the gradient energy penalty and the strain energy penalty. Because the change in equilibrium composition is much larger than that of the cell volume, as seen in part a of Figure 3 and part a of 4, we expect that the contribution of strain is relatively small compared to the concentration gradient.

The results of the calculations, shown in part a of Figure 3, are in excellent agreement with the experimentally observed decrease of the miscibility gap. Although simplifying assumptions are made, this demonstrates that the diffuse interface is a primary factor that determines the solubility limits in nano sized Li_xFePO_4, and most likely is at least partly responsible for similar observations in other insertion materials[21−23]

Interestingly, the calculations predict that for small particle sizes the lithium concentration varies throughout the whole particle in the *a* direction. This requires a reconsideration of the definition of solubility limits in these nanoparticles. The calculated solubility limits in part a of Figure 3 represent the average compositions in each phase, which due to the concentration gradient are different from the real solubility limits that are given by the concentration at the surface of the particle as illustrated by part b of Figure 3. For these small particle sizes, it is more relevant to refer to the average composition, which we will refer to as average solubility limit (ASL). This is also the right quantity for comparison with diffraction, which probes the average Li occupancy. It is arguable whether diffraction probes all lithium in the diffuse interface. The lattice plane deformation near the interface due to strain has the consequence that at least part of the interface region will not contribute to the coherently diffracted signal and is therefore not seen by diffraction.

The explanation for the shrinking miscibility gap upon particle size reduction is illustrated by the calculated concentration profiles in part b of Figure 3. In 140 nm particles, the length over which the concentration varies, dictated by the concentration gradient induced energy penalty in eq 1, is small compared to the particle size. However, in particle sizes around 35 nm the interface region covers most of the material thereby decreasing the difference in the average composition between the two coexisting Li-poor triphylite α-phase and Li-rich heterosite *β*-phase. For even smaller particles, the gradient starts to experience confinement due to the particle dimensions, which increases the concentration gradient induced energy penalty and, in competition with the homogeneous energy of mixing, leads to the shrinking miscibility gap.

The average solubility limits (ASL's) shown in part a of Figure 3 were determined at constant overall composition $Li_{\sim 0.5}FePO_4$. We further investigated the solubility limits by varying the overall compositions for different particle sizes. The experimental unit cell volume of both phases in part b of Figure 4 demonstrates that the cell volume increasingly varies with the overall composition in smaller particle size. This may be understood assuming finite

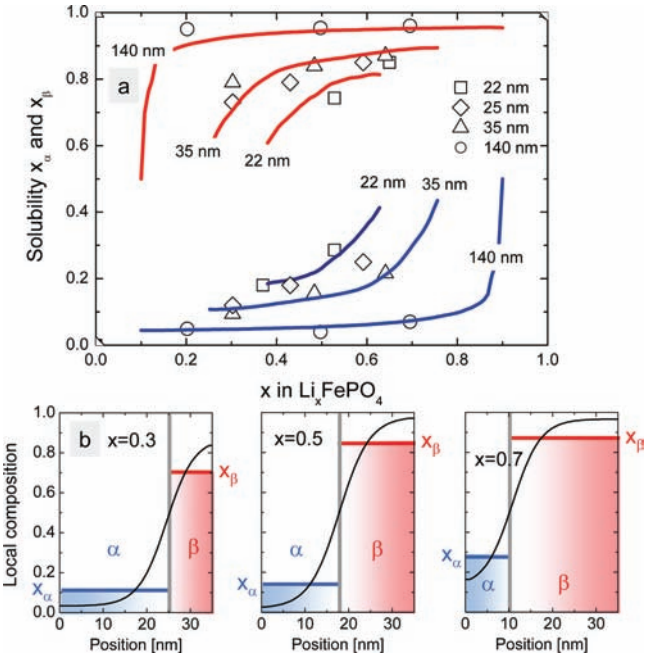

Figure 5. Measured and calculated solubility limits as a function of overall composition. (a) Symbols: Fractional lithium occupancy for both the Li-poor triphylite α-phase and the Li-rich heterosite *β*−phase representing the average solubility limits (ASL's) as a function of overall composition for different particle sizes. Lines: Calculated average compositions based on the diffuse interface model. The size of the symbols is approximately the size of the error. (b) Calculated concentration profiles based on the diffuse interface model in the *a* direction for three different overall compositions all having the same particle size 35 nm. The compositions x_α and x_β represent the average Li-compositions, referred to as average solubility limits (ASL) in the text, in the Li-poor triphylite α-phase and in the Li-rich heterosite *β*-phase, respectively.

dimensions of the stress fields generated by the phase coexistence within one coherent crystallite particle in combination with the varying phase fractions with overall composition. The lattice planes in the minority phase will be on average closer to the interface and consequently will experience more stress. At small overall compositions, $x < 0.5$, the Li-rich *β*-phase is the minority phase resulting in a relatively large decrease in cell volume compared to the increase in cell volume of the majority Li-poor α-phase. At large overall compositions, $x > 0.5$, the lithium poor phase is the minority phase resulting in a relatively large increase in cell volume, explaining the increase of the cell volume in both phases with increasing overall composition. By reducing the particle size towards the dimensions of the stress field, a larger fraction of both phases will experience strain, as was also concluded from part d of Figure 1 causing the described variation of the cell volumes with overall composition to be larger for smaller particle sizes. Because the large variation of the cell volume appears to set in below 35 nm, this indicates that the stress field typically extends over 30 nm in $LiFePO_4$.

Part a of Figure 5 reveals that for smaller particle size the measured ASL's increasingly depend on the overall composition, completely against our common knowledge based on first-order phase transitions in bulk materials where the phase compositions are independent of the overall composition. The ASL's in both the heterosite and triphylite phase increase with increasing overall composition, a trend that is more pronounced in smaller

particles. Although this qualitatively scales with the cell volume in part b of Figure 4, the change in ASL's again exceeds that assuming Vegard's law, as is deduced from part a of Figure 4, the latter including the data from part a of Figure 3 and part a of Figure 5. To explore the impact of the diffuse interface as a function of overall composition, the calculations based on eq 1 were performed for varying overall composition at a specified particle size (in contrast to the calculations in part a of Figure 3 where the particle size was varied at constant overall composition $Li_{0.5}FePO_4$). The calculated ASL's shown in part a of Figure 5 are in qualitative agreement with the experimental results, also exhibiting an increase for the ASL's of both the Li-poor (α)-phase and the Li-rich β-phase with overall composition that significantly depends on the particle size.

The origin of this effect is illustrated by the calculated concentration profiles in part b of Figure 5. When the size of the phase domain of one of the coexisting phases is on the order of the diffuse interface thickness, its ASL is invited to reduce the miscibility gap. As a consequence of the variation of the phase domain size with the overall composition, also the miscibility gap depends on overall composition. For large particles, the confinement of the diffuse interface occurs only at very small phase fractions causing the steep increase in the small and large overall composition limit. The consequence of the small phase fraction is that this steep increase in ASL's will be very hard to observe in large particles. However, in small particles the confinement of the concentration gradient takes place at much larger fractions of the material significantly influencing the ASL's at intermediate overall compositions, as observed in part a of Figure 5.

The remarkable consequence is a phase-size-diagram, relating the ASL's to the particle size, increasingly depending on the overall composition for smaller particles. Figure 6 summarizes the impact of the diffuse interface showing the calculated ASL's as a function of both particle size and overall composition. For large particle sizes, the ASL's approach a constant value, and the miscibility gap exists for almost the complete compositional range, independent of the overall composition, in agreement with common knowledge of bulk materials. However, for decreasing particle sizes the ASL's in both phases increasingly depend on the overall composition, and the miscibility gap only exists for a limited compositional range, the latter in agreement with experimental evidence.[11,16] The confinement of the diffuse interface, which increases its associated energy penalty, causes the shrinking miscibility gap. Because the dimensions of the individual heterosite and triphylite phase domains in a single particle depend on the overall composition the confinement of the diffuse interface and hence the resulting ASL depends on the overall composition. At small overall compositions, the Li-rich heterosite β-phase is the minority phase and will consequently experience the strongest confinement of the diffuse interface leading to a strongly decreased ASL. The opposite happens for the Li-poor triphylite α-phase at large overall compositions, together resulting in the asymmetric phase-size diagrams in Figure 6.

The dependence of average solubility limits (ASL's) on both particle size and overall composition fundamentally change the understanding of phase transitions in nanosized $LiFePO_4$ and nanosized insertion materials in general. When progressively inserting or extracting lithium in or from nanosized $FePO_4$ or $LiFePO_4$ respectively, the compositions in both coexisting phases will change continuously; this will require lithium transport throughout the whole particle. In contrast, changing the overall composition in bulk material only requires lithium transport near the interface. The variable ASL's also alter the dynamics in nanosized insertion materials because the diffusivity in insertion materials can change several orders of magnitude depending on the local concentration.[18−20]

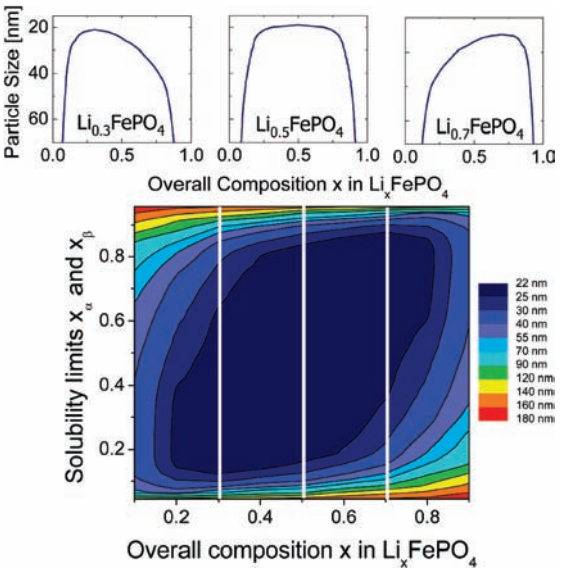

Figure 6. Calculated phase-size diagram. Calculated phase-size-diagram relating the average solubility limits (ASL's) to the overall composition for different particle sizes, the latter represented by the colored contours. The white lines represent the positions for the three sections of the phase-size diagram at different constant overall compositions, illustrating the changing phase-size diagrams with changing overall composition. Note that the section at overall composition $Li_{0.5}FePO_4$ corresponds to the results shown in part a of Figure 3.

The finding of coexisting phases within each crystallite is quite remarkable. Previously, the smallest lithiated nanosized TiO_2 anatase particles were found to have either one or the other phase, indicating that in these small crystallites the energy costly interface is avoided.[21] In a study on ~100 nm $LiFePO_4$ crystallites during charging of the battery at C/20 rate,[26] single-phased particles were observed in ex situ diffraction avoiding the phase coexistence within one particle. Although that observation at first sight may reflect the equilibrium state of individual electrode crystallites, it is a priori not clear if the charge rate is sufficiently slow for that, and if a phase front through the battery, separating Li-rich and Li-poor regions, can be excluded. That different states can be achieved electrochemically is also illustrated by a recent study where staging in electrochemical Li insertion in ~65 nm $FePO_4$ was observed.[36] In that work, it was indicated that this might be a metastable state, but comparing with the present investigation it can perhaps be stated that such half lithiated state may not be as unstable as commonly assumed, because a relatively wide interface region between the Li-rich and Li-poor phases is present. In the present investigation, the diffuse interface is essential to explain the phase behavior. This does not mean that other free-energy contributions can be excluded. For instance, surface energy contributions to the total free energy in nanomaterials can still be relevant. However, such interactions should be consistent with the coexisting phases within one particle being energetically more favorable. The forgoing illustrates that fundamental research is still required to understand this interesting and relevant group of materials.

In conclusion, the diffuse interface model, accounting for the free energy of the concentration gradient at the coherent phase boundary, is successful in explaining the experimental determined ASL's obtained by combined neutron and X-ray diffraction. Strain also gives a rational for the changes in the miscibility gap both due to particle size and composition, albeit not large enough to explain the observed results. It should be realized that the presented results apply for insertion materials in general a class of materials that plays an important role in energy storage and conversion materials. The future challenge will be to design nanoarchitectures in ionic insertion materials that minimize strain for facile nucleation, yet maximize solubility effects, both promoting the dynamic performance of insertion materials.

METHODS

Synthesis. The starting material was carbon coated $LiFePO_4$ from Phostech having an average particle size of 140 nm as determined by TEM and size broadening in diffraction. The material was ball-milled (planetary ball mill, Fritsch Pulverisette 6, using stainless steel bowls and balls) under Argon atmosphere for various times at different rotation speeds to achieve different particle sizes down to 22 nm (22 nm: 90 min, 300 rpm and 90 min 450 rpm; 25 nm: 90 min, 300 rpm and 30 min 450 rpm; 35 nm: 90 min, 300 rpm; 70 nm: 15 min, 300 rpm). The ball milling was performed in short periods of ~10 min with intermediate pauses to prevent heating of the materials. For the different particle sizes, various compositions Li_xFePO_4 were prepared by chemical oxidation of $LiFePO_4$ using nitronium tetrafluoroborate NO_2BF_4 (Aldrich >95%) as an oxidizing agent. NO_2BF_4 was dissolved in acetonitrile before adding the $LiFePO_4$ powder, and stirred for 36−48 h, all under Argon atmosphere. The mixture was washed several times with acetonitril and dried, yielding $FePO_4$ as starting material. For synthesis of Li_xFePO_4 $FePO_4$ was dispersed in hexane before very slowly adding diluted *n*-butyllithium in hexane (in the course of approximately 20 min) while stirring for a few days to ensure homogeneous lithiation. The fact that two-phase coexistence is achieved clearly indicates the lithiation was very homogeneous. If not, part of the material may be expected to be completely lithiated and part not, which was not observed in the diffraction. After washing thoroughly with hexane the materials were dried and stored under argon. Overall compositions were determined by wet chemical inductively coupled plasma spectroscopy (ICP) analysis (ratio Li:Fe).

XRD, Neutron Diffraction, and Rietveld Refinement. X-ray diffraction data were collected on a Panalytical X-pert pro using X-ray radiation from a Cu-anode (0.4×12 mm^2 line focus, 45 kV, 40 mA). To avoid air exposure, diffraction data were collected on samples in sealed holders under argon atmosphere.

The room temperature neutron diffraction measurements were performed at POLARIS and GEM, the medium-resolution high-intensity time-of-flight (TOF) diffractometers at the ISIS pulsed neutron source (Rutherford Appleton Laboratory, U.K.). In addition some of the experiments were repeated at various constant wave neutron diffraction instruments: D20 at the ILL, HRPT at PSI and Wombat at ANSTO. The samples for neutron diffraction were loaded in an argon atmosphere into airtight vanadium sample containers sealed with indium O-rings. The resulting neutron diffraction patterns were refined using the Rietveld method as implemented in *GSAS*.[37] Besides the atomic and lattice parameters and line-broadening parameters, the crystal phase fractions, and background were fitted. The fitting procedure of the TOF patterns (POLARIS and GEM) included two neutron banks (under 90° and 145° with respect to the incident beam, equally weighted), which were simultaneously fitted with X-ray data on the same material. For neutron TOF diffraction the incident wavelength is less well defined than the X-ray data, thus the simultaneous fit was restricted to the lattice parameters from fitting the X-ray data. This was achieved by allowing the neutron diffractometer constants to vary (effectively the exact sample position in the neutron flight path). To correct for an error in the vertical alignment, a diffractometer constant zero term was fitted. The natural abundance of ^{6}Li necessitated the neutron data be corrected for a wavelength dependent absorption correction based on the Li-density and dimensions of the sample containers, commonly used for TOF neutron diffraction. To prevent correlation effects, the anisotropic Li temperature factors for Li in both heterosite and triphylite phases were fixed to those resulting from fitting the 140 nm $LiFePO_4$ material leading to displacement ellipsoids elongated toward the proposed curved 1D lithium diffusion path.[30−32] Combined X-ray and neutron diffraction refinements were performed using the *GSAS* program[37] with the EXPGUI interface.[38] The background of the neutron data was fitted with 9 terms (function type 4 in *GSAS*), and the X-ray data was fitted with 7 terms (function type 1 in *GSAS*). Both the neutron and the X-ray diffraction line shape were fitted using function type 4 in *GSAS*. This accounts for anisotropic strain broadening described by a semiempirical form for orthorhombic $LiFePO_4$ using the Laue class *mmm*. Additionally, the isotropic particle size broadening was refined indicating increased size broadening compared to the pristine particle size for overall compositions between 0 and 1, as seen in the Supporting Information. All refinements resulted in residuals R_{wp} and R_{exp} less than 3%, which indicates an excellent fit. Detailed fit parameters are included in the Supporting Information for a number of samples.

Calculations Diffuse Interface. For the impact of the free energy due to the diffuse interface described in eq 1, a regular solution model for the homogeneous free energy $g_{hom}(c) = \omega c(1-c) + k_BT[c \ln c + (1-c) \ln (1-c)]$ is assumed[13,25] where the first term represents the enthalpy and the second term the entropy of mixing. The interaction parameter ω was chosen to be $5k_BT$, which is considered as a reasonable approximation for $LiFePO_4$.[13,39] The quantity $\lambda_i \equiv (K_{ii}/K_BT)^{1/2}$ has the units length and represent the length scales for the interphasial widths in the different eigendirections.[13,34] More precisely, the interphasial width scales as $L_i \equiv \lambda_i(K_BT/\omega)^{1/2}$.[13] Experimental evidence in Li_xFePO_4 shows the phase boundary is always in the *bc* plane,[27] as confirmed by the observed anisotropic strain broadening in part c of Figure 1 minimizing its elastic energy.[24,27] As a consequence, the concentration can be assumed to vary only in the *a* direction, in which direction the interphasial width λ was observed to be approximately 4 nm,[27,28] which allows to estimate K (which reduces to a scalar for this 1D case). To calculate the 1D equilibrium concentration profile, and the average solubility limits, mass transport was allowed to smooth away differences in the chemical potential based on the free energy in eq 1. Two boundary conditions should be obeyed, mass conservation and the variational boundary condition $\hat{n}K\nabla c = 0$, which guarantees continuity of the chemical potential at the surface of the particle. Variation of the particle size and the overall composition is easily achieved by the initial value of the concentration profile, which was initially chosen to be a step function.

ASSOCIATED CONTENT

Supporting Information. Detailed parameters resulting from the simultaneous fitting of the neutron and X-ray diffraction data on the materials having particle sizes 140, 35, and 22 nm with composition $Li_{0.5}FePO_4$. In addition it contains the domain size broadening for the 35 nm material as a function of overall composition. This material is available free of charge via the Internet at http://pubs.acs.org.

AUTHOR INFORMATION

Corresponding Author
m.wagemaker@tudelft.nl

■ ACKNOWLEDGMENT

This work is a contribution from the Delft Energy Initiative (DEI). Financial support from Shell is acknowledged for the Sustainable Mobility grant funding D.P.S. The Netherlands Organization for Scientific Research (NWO) is acknowledged for both beam time at ISIS and the CW-VIDI grant of M.W. The authors thank Ron Smith for assistance with the neutron diffraction experiments at POLARIS (ISIS), Michela Brunelli and Mark Johnson at D20 (ILL), and Vladimir Pomjakushin at HRPT (PSI). We thank the Alistore network for providing access to the TEM measurements.

■ REFERENCES

(1) Padhi, A. K.; Nanjundaswamy, K. S.; Goodenough, J. B. *J. Electrochem. Soc.* **1997**, *144*, 1188–1194.
(2) Chung, S. Y.; Bloking, J. T.; Chiang, Y. M. *Nat. Mater.* **2002**, *1*, 123–128.
(3) Huang, H.; Yin, S. C.; Nazar, L. F. *Electrochem. Solid-State Lett.* **2001**, *4*, A170–A172.
(4) Delacourt, C.; Poizot, P.; Levasseur, S.; Masquelier, C. *Electrochem. Solid-State Lett.* **2006**, *9*, A352–A355.
(5) Jamnik, J.; Maier, J. *Phys. Chem. Chem. Phys.* **2003**, *5*, 5215–5220.
(6) Van der Ven, A.; Wagemaker, M. *Electrochem. Commun.* **2009**, *11*, 881–884.
(7) Hill, T. L. *Thermodynamics of Small Systems*; W.A. Benjamin: New York, 1963.
(8) Delacourt, C.; Poizot, P.; Tarascon, J. M.; Masquelier, C. *Nat. Mater.* **2005**, *4*, 254–260.
(9) Zhou, F.; Marianetti, C. A.; Cococcioni, M.; Morgan, D.; Ceder, G. *Phys. Rev. B* **2004**, *69*.
(10) Meethong, N.; Huang, H. Y. S.; Speakman, S. A.; Carter, W. C.; Chiang, Y. M. *Adv. Funct. Mater.* **2007**, *17*, 1115–1123.
(11) Kobayashi, G.; Nishimura, S. I.; Park, M. S.; Kanno, R.; Yashima, M.; Ida, T.; Yamada, A. *Adv. Funct. Mater.* **2009**, *19*, 395–403.
(12) Yamada, A.; Koizumi, H.; Nishimura, S. I.; Sonoyama, N.; Kanno, R.; Yonemura, M.; Nakamura, T.; Kobayashi, Y. *Nat. Mater.* **2006**, *5*, 357–360.
(13) Burch, D.; Bazant, M. Z. *Nano Lett.* **2009**, *9*, 3795–3800.
(14) Wagemaker, M.; Mulder, F. M.; van der Ven, A. *Adv. Mater.* **2009**, *21*, 1–7.
(15) Dodd, J. L.; Yazami, R.; Fultz, B. *Electrochem. Solid-State Lett.* **2006**, *9*, A151–A155.
(16) Meethong, N.; Huang, H. Y. S.; Carter, W. C.; Chiang, Y. M. *Electrochem. Solid-State Lett.* **2007**, *10*, A134–A138.
(17) Stevens, R.; Dodd, J. L.; Kresch, M. G.; Yazami, R.; Fultz, B.; Ellis, B.; Nazar, L. F. *J. Phys. Chem. B* **2006**, *110*, 22732–22735.
(18) Van der Ven, A.; Ceder, G.; Asta, M.; Tepesch, P. D. *Phys. Rev. B* **2001**, *64*, 17.
(19) Van der Ven, A.; Ceder, G. *J. Power Sources* **2001**, *97−8*, 529–531.
(20) Van der Ven, A.; Thomas, J. C.; Xu, Q. C.; Swoboda, B.; Morgan, D. *Phys. Rev. B* **2008**, 78.
(21) Wagemaker, M.; Borghols, W. J. H.; Mulder, F. M. *J. Am. Chem. Soc.* **2007**, *129*, 4323.
(22) Schimmel, H. G.; Huot, J.; Chapon, L. C.; Tichelaar, F. D.; Mulder, F. M. *J. Am. Chem. Soc.* **2005**, *127*, 14348–14354.
(23) Borghols, W. J. H.; Wagemaker, M.; Lafont, U.; Kelder, E. M.; Mulder, F. M. *Chem. Mater.* **2008**, *20*, 2949–2955.
(24) Van der Ven, A.; Garikipati, K.; Kim, S.; Wagemaker, M. *J. Electrochem. Soc.* **2009**, *156*, A949–A957.
(25) Singh, G. K.; Ceder, G.; Bazant, M. Z. *Electrochim. Acta* **2008**, *53*, 7599–7613.
(26) Delmas, C.; Maccario, M.; Croguennec, L.; Le Cras, F.; Weill, F. *Nat. Mater.* **2008**, *7*, 665–671.
(27) Chen, G. Y.; Song, X. Y.; Richardson, T. J. *Electrochem. Solid-State Lett.* **2006**, *9*, A295–A298.
(28) Laffont, L.; Delacourt, C.; Gibot, P.; Wu, M. Y.; Kooyman, P.; Masquelier, C.; Tarascon, J. M. *Chem. Mater.* **2006**, *18*, 5520–5529.
(29) Gibot, P.; Casas-Cabanas, M.; Laffont, L.; Levasseur, S.; Carlach, P.; Hamelet, S.; Tarascon, J. M.; Masquelier, C. *Nat. Mater.* **2008**, *7*, 741–747.
(30) Nishimura, S.; Kobayashi, G.; Ohoyama, K.; Kanno, R.; Yashima, M.; Yamada, A. *Nat. Mater.* **2008**, *7*, 707–711.
(31) Islam, M. S.; Driscoll, D. J.; Fisher, C. A. J.; Slater, P. R. *Chem. Mater.* **2005**, *17*, 5085–5092.
(32) Morgan, D.; Van der Ven, A.; Ceder, G. *Electrochem. Solid-State Lett.* **2004**, *7*, A30–A32.
(33) Jacob, K. T.; Raj, S.; Rannesh, L. *Int. J. Mater. Res.* **2007**, *98*, 776–779.
(34) Cahn, J. W.; Hilliard, J. E. *J. Chem. Phys.* **1958**, *28*, 258–267.
(35) Kittel, C. *Solid State Physics*; Wiley: New York, 1995.
(36) Gu, L.; Zhu, C. B.; Li, H.; Yu, Y.; Li, C. L.; Tsukimoto, S.; Maier, J.; Ikuhara, Y. *J. Am. Chem. Soc.* **2011**, *133*, 4661–4663.
(37) Larson, A. C. *GSAS*; Los Alamos National Laboratory, 1994.
(38) Toby, B. H. *J. Appl. Crystallogr.* **2001**, *34*, 210.
(39) Han, B. C.; Van der Ven, A.; Morgan, D.; Ceder, G. *Electrochim. Acta* **2004**, *49*, 4691–4699.